

**Kohn anomaly and elastic softening in body-centered cubic molybdenum at high pressure**Chao Yang<sup>1,2</sup>, Youjun Zhang<sup>3,\*</sup>, Nilesh P. Salke<sup>4</sup>, Yan Bi<sup>5</sup>, Ahmet Alatas<sup>6</sup>, Ayman H. Said<sup>6</sup>, Jiawang Hong<sup>2,†</sup> and Jung-Fu Lin<sup>7,‡</sup><sup>1</sup>*Department of Physics, Jishou University, Hunan 416000, China*<sup>2</sup>*School of Aerospace Engineering, Beijing Institute of Technology, Beijing 100081, China*<sup>3</sup>*Institute of Atomic and Molecular Physics, Sichuan University, Chengdu 610065, China*<sup>4</sup>*Department of Physics, University of Illinois Chicago, Chicago, Illinois 60607, USA*<sup>5</sup>*Center for High Pressure Science and Technology Advanced Research (HPSTAR), Shanghai 201900, China*<sup>6</sup>*Argonne National Laboratory, Lemont, Illinois 60439, USA*<sup>7</sup>*Department of Geological Sciences, Jackson School of Geosciences, The University of Texas at Austin, Austin, Texas 78712, USA*

(Received 6 October 2021; revised 13 February 2022; accepted 22 February 2022; published 9 March 2022)

Transition metals in body-centered cubic (bcc) structures under compression can display several novel physical properties because of their complex electronic structures and electron-phonon interactions. Here, we used inelastic x-ray scattering experiments in a diamond-anvil cell up to  $\sim 45$  GPa and density-functional theory calculations up to 210 GPa to investigate the phonon dispersions, and electronic and elastic properties of single-crystal molybdenum (Mo). Our results show a pressure-induced Kohn anomaly at  $q \sim 0.5$  along the  $[\xi 00]$  direction in the longitudinal acoustic mode at  $\sim 45$  GPa; this anomaly is triggered by the pressure-enhanced Fermi-surface nesting effect. Theoretical calculations show that electron redistributions in the  $s$ -to- $d$  orbitals of bcc-Mo contribute to the shear modulus anomaly at  $\sim 50$  GPa. In contrast, the Young's modulus anomaly in bcc-Mo at  $\sim 210$  GPa results from a Lifshitz-type electronic topological transition. Our results shed light on the complex electronic behaviors that are associated with macroscopic elastic properties in typical bcc  $d$ -block transition metals under compression.

DOI: [10.1103/PhysRevB.105.094105](https://doi.org/10.1103/PhysRevB.105.094105)**I. INTRODUCTION**

Physical properties of  $d$ -block transition metals are of great interest to leading-edge research of materials science, condensed-matter physics, and planetary science [1–4]. It has been reported that a number of intriguing properties (such as superconductivity, electronic and structural phase transitions, phonon anomalies, and elastic softening) occur in  $d$ -block transition metals when they are under pressure [5–9]. Many of those exotic properties are related to the  $d$ -band occupancy according to the cohesive energy mechanism in one-electron theory [10]. For example, elastic constants of cubic transition metals vary with an increase in their atomic numbers; this can be understood in terms of the  $s$ -to- $d$  electronic transition at ambient conditions (e.g., Ta, W, and Pt [11]). The bulk modulus of lanthanum displays an anomalous stiffening, and this is typically caused by the termination of increased  $d$ -band filling at elevated pressures [12,13]. Recent advanced theoretical calculations and experimental studies revealed novel physical mechanisms that can contribute to elastic and mechanical anomalies in  $d$ -block transition metals with body-centered cubic (bcc) crystal structure when they are under high pressure. These anomalies include Fermi surface nesting, band Jahn-

Teller distortion, and electronic topological transitions [9,14–16]. Particular examples include electronic topological transitions (ETT) of bcc-Ta and bcc-Nb at high pressures; these are associated with their elastic moduli anomalies [17,18]. In a nutshell, the electron-phonon coupling effect, ETT, and band Jahn-Teller distortions are mostly related to the modifications and interactions of  $d$  orbitals in  $d$ -block transition metals that are under compression. Therefore, it is important to investigate interactions between electronic structures (especially the  $d$ -orbital electronic structures) and lattice dynamics of transition metals to better understand their physical manifestations in elastic, mechanical, and transport properties when under compression.

Mo is a typical bcc transition metal. Previous investigations regarding the lattice dynamics of Mo at high pressure revealed a series of physical anomalies, such as anomalous changes in the  $H$  point [19] and  $L[\xi\xi\xi]$  branch in the vicinity of  $\xi = 2/3$  [20–22]. In particular, Farber *et al.* used high-resolution inelastic x-ray scattering in a diamond-anvil cell and theoretical calculations to study the  $H$ -point phonon anomaly. Their experimental phonon-dispersion curves along the  $\Gamma$ - $H$  direction at 17 GPa did not show a phonon anomaly beyond the  $H$  point. Along with theoretical calculations, the curves indicate that the  $H$ -point anomaly in Mo is a result of strong electron-electron coupling. This explanation, however, is at odds with previous reports for other bcc crystal structures, such as V, Ta, and Nb, which are adjacent to Mo on the periodic table. Phonon dispersions of V, Ta, and Nb at the  $H$  point do not

\*zhangyoujun@scu.edu.cn

†hongjw@bit.edu.cn

‡afu@jsg.utexas.edu

show any anomalies under ambient or high-pressure conditions [14,18,23], but their phonon anomalies occur between the  $\Gamma$  point and  $H$  point along the  $\Gamma$ - $H$  direction at ambient or high-pressure conditions. Therefore, further investigations regarding the phonon dispersions and possible anomalies of single-crystal bcc-Mo under high pressure can aid our understanding of the lattice dynamics in  $d$ -block bcc metals.

The elasticity and mechanical properties of bcc-Mo under high pressure are also of significant interest in condensed-matter physics and can be linked to the aforementioned electronic structures. Mo is often used as a refractory material because it has high thermal stability and as a pressure calibrant because it has well-measured elasticity [19,24–26]. However, shear modulus softening of Mo has been observed at  $\sim 210$  GPa along the Hugoniot in shock compression experiments. Interestingly, the underlying mechanism behind the anomaly remains debated [27–31]. Hixson *et al.* [27] proposed that the shear softening anomaly at  $\sim 210$  GPa results from a phase transition from bcc to hexagonal closed packed (hcp). However, more recent shock experiments did not find statistically significant evidence to support the bcc-to-hcp phase transition in the range of this pressure [28,29,32]. *In situ* x-ray diffraction experiments under laser shock compression were conducted and further confirmed that bcc-Mo remains stable before shock-induced melting [33]. Further studies on the elastic properties of single-crystal Mo can also be used to elucidate its electronic and phononic properties under high pressures.

In this work, high-energy resolution inelastic x-ray scattering (HERIX) spectrometer along the high-symmetric  $\Gamma$ - $H$  [ $\xi 00$ ] and  $\Gamma$ - $N$  [ $\xi \xi 0$ ] directions was used to measure acoustic phonon dispersions of single-crystal Mo at hydrostatic pressures up to  $\sim 45$  GPa and at room temperature. We also used density-functional theory (DFT) to compute phonon dispersions of Mo, and the results match the experimental results well. Kohn anomalies in the longitudinal branch along the  $\Gamma$ - $H$  direction were observed at  $\sim 45$  GPa, and their magnitudes were enhanced with an increase in pressure. Our DFT calculations show that the Kohn anomalies are related to the Fermi-surface nesting and the electron-phonon coupling effect at high pressure. We also observed anomalies of elastic constants caused by the  $s$ -to- $d_{xz}/d_{yz}$  electronic transition about 50 GPa, where the elastic anomalies at approximately 210 GPa originate from the electronic topological transition.

## II. METHODS

Molybdenum single crystals, which had an initial size of  $\sim 500 \mu\text{m}$  long and  $\sim 150 \mu\text{m}$  thick in the (100) orientation, were purchased from Princeton Scientific Corporation, USA. A few pieces of smaller crystals, which were  $40 \times 50 \mu\text{m}^2$  in size and  $15 \mu\text{m}$  thick, were cut from the original large crystals using a focused ion beam (FIB) (FEI VERSA 3D type); cuts were made at the Center for High Pressure Science and Technology Advanced Research (HPSTAR), Shanghai [24]. A gallium ion beam with a current of 15 nA was used for the FIB cutting to reduce potential damage to the quality of the single crystal. Before HERIX experiments, the quality and lattice parameters of the single crystal before and after loading into diamond-anvil cells (DACs) were checked using

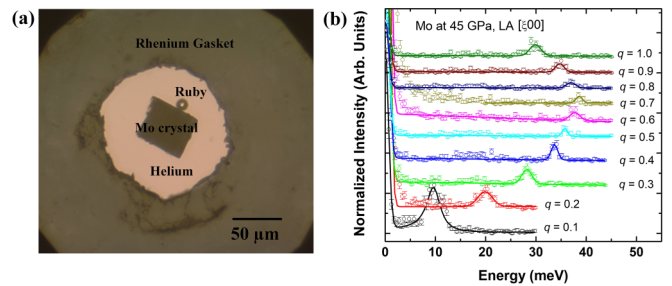


FIG. 1. High-energy resolution inelastic x-ray scattering experiments in single-crystal Mo at high pressure. (a) Microphotograph of a Mo crystal loaded with He in a DAC at 45.0(0.5) GPa. The sample was  $\sim 40 \times 50 \mu\text{m}$  long and  $\sim 15 \mu\text{m}$  thick. The culet size of the diamond anvils was  $300 \mu\text{m}$ . (b) Representative longitudinal acoustic (LA) spectra of Mo at 45.0(0.5) GPa measured in the (200) Brillouin zone along the  $[\xi 00]$  direction from  $q = 0.1$  to  $q = 1.0$ . Error bars (vertical ticks) were estimated from counting statistics. Solid lines were fit to experimental data (open circles) using a Gaussian function. An additional Gaussian function was used for the elastic line centered around 0 meV.

x-ray diffraction (XRD) at the 13ID-D station, GeoSoilEnvi-roConsortium for Advanced Radiation Sources (GSECARS) of the Advanced Photon Source (APS), Argonne National Laboratory. Analysis of the measured XRD patterns of the FIB-cut crystals showed that the crystals displayed sharp and circular diffraction spots with a typical full width at half maximum (FWHM) of  $0.09^\circ$  [18]. A crystal platelet in the (100) orientation was loaded into a short symmetric DAC with an x-ray opening of  $90^\circ$  ( $2\theta$ ). The DAC was equipped with a pair of diamonds that had  $250\text{-}\mu\text{m}$  culets [Fig. 1(a)]. A rhenium gasket that had an initial thickness of  $250 \mu\text{m}$  was preindented to a depth of approximately  $30 \mu\text{m}$ , and a hole with a diameter of  $160 \mu\text{m}$  was then drilled into the gasket and used as a sample chamber. Helium was used as a pressure medium to provide a quasi-hydrostatic condition for the crystal in the sample chamber. A ruby sphere was loaded near the crystal and served as a pressure calibrant according to the ruby fluorescence pressure scale [34]. The pressure of the sample chamber was double checked using the equation of state of the Mo sample on the basis of the analysis of *in situ* x-ray diffraction patterns [35]. More experimental details can be found elsewhere [18].

Experimental measurements of high-pressure phonon dispersions of Mo were carried out using the HERIX instruments at Sector 30 of the APS [36–39]. An incident x-ray source with an energy of 23.724 keV and an energy resolution of 1.4 meV was focused down to a beam size of  $35 \times 15 \mu\text{m}^2$  on the sample. An online x-ray diffraction setup at Sector 30 of the APS was used to orient and align Mo crystals with (110), (200), and (220) diffraction spots. A spherically bent silicon crystal analyzer of the (12 12 12) reflection was used in the system to collect the longitudinal and transverse modes along the high-symmetric  $[\xi 00]$  and  $[\xi \xi 0]$  directions [40]. A typical collection time of about 1 to 2 h was used to detect a set of the phonon signals. For each scan in constant- $q$  scans, HERIX energy spectra were measured at 22.0(0.5) GPa and 45.0(0.5) GPa over the energy range of  $\pm 40$  meV with a step size of 0.25 or 0.5 meV. Representative spectra in the longitudinal acoustic

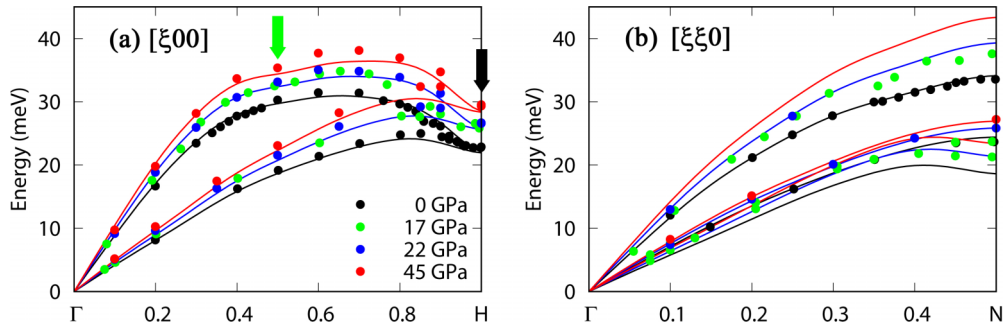


FIG. 2. Phonon dispersions in bcc single-crystal Mo at high pressure along the (a)  $\Gamma$ - $H$  and (b)  $\Gamma$ - $N$  directions. Blue and red solid circles represent our experimental data at 22 and 45 GPa, respectively, while black and green solid circles represent results at ambient condition and at 17 GPa from previous inelastic neutron and x-ray scattering measurements [19,56]. Errors for data are smaller than the circle size and are not plotted for clarity. Black, blue, and red lines represent DFT calculations of phonon dispersions at 0, 22, and 45 GPa, respectively. Longitudinal dispersions along the  $\Gamma$ - $N$  direction in experiments at 45 GPa were not completed because of an anvil failure. Dark-green and black arrows indicate the Kohn anomalies at  $q \sim 0.5$  and near the  $H$  point, respectively.

mode in the Brillouin zone (200) along the  $[\xi 00]$  direction are shown in Fig. 1(b). The spectra were fitted using a Gaussian function with the DAVE2 Program to extract energy values and FWHMs of the phonons [41].

First-principles calculations were made using the Vienna *Ab initio* Simulation Package (VASP) [42–44]. A kinetic energy cutoff of 350 eV and a  $30 \times 30 \times 30$   $\Gamma$ -centered  $k$ -point mesh was used for primitive cell simulations. Phonon dispersions were calculated using the PHONOPY code [45] with  $6 \times 6 \times 6$  supercells, and elastic constants were calculated using density-functional perturbation theory (DFPT). The projector augmented-wave (PAW) approximation and local density approximation (LDA) were used to describe the atomic electronic structures [46,47]. LOBSTER code was used to calculate the electron occupancy of each orbital [48]. Three-dimensional Fermi-surface structures were simulated using the VASP and WANNIER90 codes [49] and were visualized using the XCRYSDEN package [50]. Electron-phonon interaction properties were calculated using DFPT as implemented in the ABINIT code with a PAW pseudopotential within LDA for the exchange-correlation function [51,52]. A  $\Gamma$ -centered  $k$  grid of  $36 \times 36 \times 36$  and a  $12 \times 12 \times 12$   $q$ -point mesh, a Gaussian smearing of 0.01 Ha, and a cutoff energy of 25 Ha were used for the electron-phonon coupling coefficient and Fermi-surface nesting function calculations. Atomic orbital projected 3D Fermi surfaces were calculated using the QUANTUM ESPRESSO package [53] and then visualized using the FERMISURFER code [54]. For the PAW pseudopotential within LDA for the exchange-correlation function, a plane-wave cutoff of 50 Ry and a  $30 \times 30 \times 30$   $\Gamma$ -centered  $k$ -point mesh was used to describe the electronic structures. The convergence of these calculations is carefully checked to balance the accuracy and computational cost (see Fig. S1 in the Supplemental Material [55]).

### III. RESULTS AND DISCUSSION

Phonon dispersions of single-crystal Mo along the high-symmetry directions  $\Gamma$ - $H$  and  $\Gamma$ - $N$  at high pressure are shown in Fig. 2; previous data at gathered at ambient conditions using inelastic neutron scattering measurement [56] as well as our DFT calculations (which agree with the experimental results)

are also shown. Overall, the measured phonon energies increase at elevated pressures. A Kohn anomaly near the  $H$  point was observed at each pressure, and this is consistent with the previous report [19] (Fig. 2). Interestingly, in addition to the  $H$ -point phonon anomaly, we found another Kohn anomaly of Mo at  $q \sim 0.5$  along the  $[\xi 00]$  direction in the LA mode; this anomaly starts to show a kink at  $\sim 45$  GPa, which is the highest pressure we reached in our measurements.

We performed first-principles calculations of phonon dispersions at pressures up to 210 GPa to investigate the Kohn anomaly at pressures beyond the current experiments, and the results are shown in Fig. 3(a). At higher pressures (such as 210 GPa), the kink at  $q \sim 0.5$  along the  $[\xi 00]$  direction of the LA mode becomes very distinct, and this confirms the pressure-enhanced Kohn anomaly. In contrast, the Kohn anomaly near the  $H$  point becomes weaker with an increase in the pressure. To show the strength of the Kohn anomaly, we further calculated the phonon-frequency ratio, which is defined as the phonon frequency at the  $H$  point ( $q = 1.0$ ) divided by the maximum value along  $\Gamma$ - $H$  (at  $q \sim 0.65$ ). As shown in Table I, this ratio gradually increased with compression, and this indicates that the Kohn anomaly near the  $H$  point gradually collapsed with an increase in the pressure. The continuous weakening of the  $H$ -point Kohn anomaly at high pressure is consistent with previous observations [19], in which a significantly decreased  $H$ -point anomaly was observed in both high-resolution inelastic x-ray scattering (IXS) experiments and in DFT calculations.

The  $q$ -dependent electron-phonon coupling (EPC) coefficient and the Fermi-surface nesting function were calculated to illustrate the nature of the observed Kohn anomalies in compressed Mo; the results are shown in Figs. 3(b) and 3(c). Results of the first-principles calculations show that the magnitude of the EPC coefficient at the  $H$  point is as high as  $\sim 0.7$  at ambient pressure. In contrast, it continuously decreased to  $\sim 0.5$  when the pressure was increased to  $\sim 100$  GPa [Fig. 3(b)], and this confirms a previous report [18]. However, the anomaly at  $q \sim 0.5$  along the  $\Gamma$ - $H$  direction did not originate from the EPC because the EPC coefficient did not change significantly upon compression. Instead, the Fermi-surface nesting function increased obviously at  $q \sim 0.5$  [Fig. 3(c)]. Therefore, the Kohn anomaly of Mo at  $q \sim 0.5$  under high

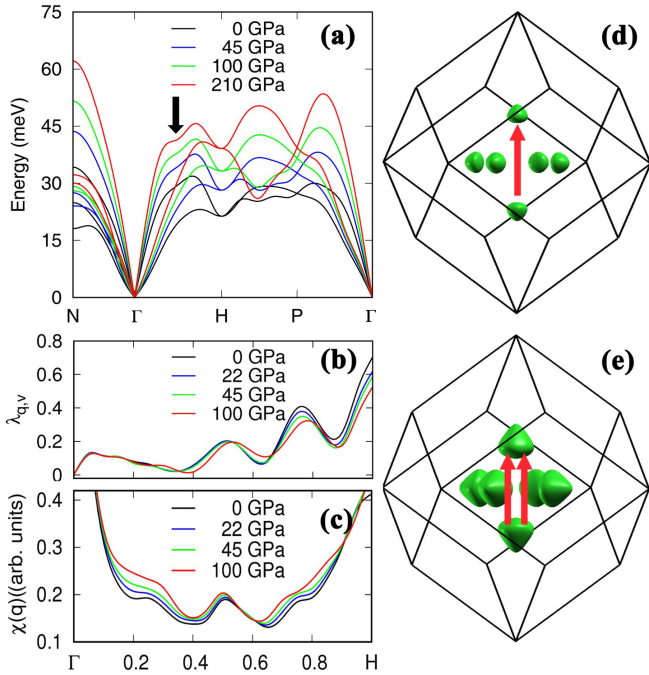


FIG. 3. DFT results of phonon dispersions, electron-phonon coupling, Fermi surface nesting, and 3D Fermi surfaces in bcc Mo under pressure. (a) Calculated phonon dispersions at pressures of 0–210 GPa. The black arrow indicates the Kohn anomalies of bcc Mo at  $q \sim 0.5$  along the  $\Gamma$ - $H$  direction. Electron-phonon coupling coefficients ( $\lambda_{q,v}$ ) (b) and Fermi-surface nesting functions [ $\chi(q)$ ] (c) in bcc Mo along the  $\Gamma$ - $H$  direction at high pressures of 0–100 GPa. Three-dimensional Fermi surfaces of bcc Mo are shown at (d) 0 GPa and (e) 210 GPa. Red arrows indicate the Fermi-surface nesting vectors along the  $\Gamma$ - $H$  direction. The 3D Fermi surface structures simulated with VASP and WANNIER90 were visualized using XCRYSDEN [50].

pressure was most likely induced by the pressure-enhanced Fermi surface nesting, which has a strong electronic screening effect on phonon dispersions [57]. Three-dimensional Fermi surfaces at ambient and 210 GPa were also calculated, and the results are shown in Figs. 3(d) and 3(e), respectively. The topology of the Fermi surfaces shows that two areas the Fermi surfaces are nearly flat and are enlarged under compression [as indicated by the red arrows in Fig. 3(e)]. This indicates that there is an enhanced Fermi-surface nesting effect at high pressures. These results are similar to the observation of a Kohn anomaly in bcc-Ta at  $q \sim 0.7$  in the same direction, even at 0 GPa [18,58]; in this case, the Kohn anomaly is also enhanced by the Fermi-surface nesting effect.

The elastic constants of the cubic single-crystal Mo can be extracted from the velocity of phonon modes that travel along the high-symmetry directions [59]. For example,  $C_{11}$  can be

derived using the following equation:

$$v_L = \sqrt{\frac{C_{11}}{\rho}}, \quad (1)$$

where  $v_L$  is the longitudinal phonon velocity along the [100] direction near the  $\Gamma$  point,  $C_{11}$  is the elastic constant along the same direction, and  $\rho$  is the material density. Linear fitting to the phonon dispersion in  $Q$ - $E$  (momentum-energy) measurements near the  $\Gamma$  point (Table II) were used to extract full elastic constants ( $C_{ij}$ ) of the Mo crystal from HERIX experiments that were conducted about ambient, 22 GPa, and 45 GPa. We also calculated the elastic moduli using first-principles calculations up to 240 GPa. Except for the calculated  $C_{11}$ , which was systematically higher by  $\sim 17\%$  than the measured data [26], the experimental and calculated results are in good agreement with each other. The overestimation of  $C_{11}$  may occur because LDA calculations overall underestimate the lattice parameters of Mo at high pressures (Table II) [60].

We determined the elastic moduli of bcc-Mo under compression using the measured and calculated elastic constants according to Voigt's formulas [62], which are as follows:

$$B = \frac{C_{11} + 2C_{12}}{3}, \quad (2)$$

$$G = C_{44} - \frac{1}{5}(2C_{44} + C_{12} - C_{11}), \quad (3)$$

$$\nu = \frac{C_{12} - \frac{1}{5}(2C_{44} + C_{12} - C_{11})}{2[C_{12} + C_{44} - \frac{2}{5}(2C_{44} + C_{12} - C_{11})]}, \quad (4)$$

$$E = 2(1 + \nu)G, \quad (5)$$

where  $B$  is the crystal bulk modulus,  $G$  is the shear modulus,  $\nu$  is Poisson's ratio, and  $E$  is Young's modulus. At high pressures, the DFT results are expected to be higher than the experimental results due to the following reasons [28,63,64] (Fig. 4): (a) the shear modulus and Young's modulus of Mo were calculated at 0 K, whereas the experiment results from literatures were conducted at high temperature (under shock compression). The application of high temperature usually softens the elastic modulus due to the expansion of the volume and weakening the bond-bond interactions. (b) Our DFT calculations were conducted using LDA, which usually underestimates the lattice parameters, so the atom-atom interactions become stronger and the elastic constants are overestimated. Figure 4 shows two anomalies of the shear modulus and Young's modulus; these are present in both the experimental results and DFT simulations at approximately 50 and 210 GPa (we should note that the DFT-calculated elastic anomaly located around 210 GPa may not occur at high pressure-temperature [55,65]). There is no structural phase

TABLE I. DFT-calculated volume compression and frequency shifts ratio at the  $H$  point.

Pressure (GPa)	0	22	45	100	210
Volume compression $[(V-V_0)/V_0]^a$	0%	6.32%	11.25%	19.55%	29.65%
Frequency ratio ( $\varepsilon_H/\varepsilon_{q \sim 0.65}$ )	66.90%	71.33%	74.87%	79.88%	85.65%

<sup>a</sup> $V_0$  is the volume of Mo at ambient conditions.  $\varepsilon_H/\varepsilon_{q \sim 0.65}$  is the phonon frequency at the  $H$  ( $q = 1.0$ ) or  $q \sim 0.65$  point along the  $\Gamma$ - $H$  direction.

TABLE II. IXS-measured and DFT-calculated elastic constants of Mo at high pressure (GPa).

Pressures (GPa)	Method	Lattice parameters (Å)	$C_{11}$	$C_{12}$	$C_{44}$
0	Expt. <sup>a</sup>	3.147	465.0(0.6)	163.0(2.0)	109.0(0.9)
	DFT	3.113	512.8	180.8	104.2
22(0.5)	Expt.	3.073(1)	534(9)	203(11)	145(4)
	DFT	3.046	621.6	228.4	135.3
45(0.8)	Expt.	3.012(1)	604(5)	250(16)	166(3)
	DFT	2.992	710.9	281.0	155.7
100	DFT	2.895	862.0	399.4	175.5
200	DFT	2.778	1140.2	598.8	262.5
240	DFT	2.743	1253.0	666.9	307.4

<sup>a</sup>Reference [61].

transition in bcc-Mo at high pressures up to at least 420 GPa (0 K), according to previous DFT-calculated results [27,66]. Besides, the solid-to-liquid phase transition occurs at pres-

ures above  $\sim 240$  GPa under shock compression [28]. Therefore, the softening of the two elastic moduli that occur around 50 and 210 GPa may not be attributed to any known structural phase transitions in Mo.

We first investigated the number of  $s$  and  $d$  orbital electrons in Mo at high pressures to understand the physical mechanisms of the aforementioned elastic modulus anomalies [48]. Our results show that the number of  $s$ -orbital electrons in Mo decreased, whereas the number of  $d$  orbital electrons increased with an increase in pressure [Figs. 5(a)–5(c)], and this indicates a pressure-induced  $s$ -to- $d$  electronic transition [67]. The  $d_{xy}$  and  $d_{yz}$  orbitals, which are closer to the Fermi surface, display anomalies more clearly at around 50 GPa [Fig. 5(b)] because of crystal-field splitting of the  $d$  orbitals in the bcc structure. Therefore, these elastic moduli anomalies are likely related to the  $d$ -band filling mechanism [12,13].

Canonical band theory with the atomic-sphere approximation can be used to understand the relationship between the elastic moduli and the  $s$ -to- $d$  electronic transition [12]. It can be described as [12,68,69]

$$3BV \sim 3B_0V + \left[ \left( \frac{\delta \varepsilon}{\delta \ln S} \right)_s - \left( \frac{\delta \varepsilon}{\delta \ln S} \right)_d \right] \left( \frac{dn_s}{d \ln V} \right), \quad (6)$$

where  $V$  is the volume,  $S$  is the Wigner-Seitz radius ( $\frac{4}{3}\pi S^3 = V$ ),  $dn_s$  is the change in the number of the  $s$  orbital electrons,  $\varepsilon$  is the band energy, and  $B_0$  (positive) is the bulk modulus in the absence of an electronic transition ( $dn_s = 0$ ). The second term on the right-hand side of Eq. (6),  $[(\frac{\delta \varepsilon}{\delta \ln S})_s - (\frac{\delta \varepsilon}{\delta \ln S})_d](\frac{dn_s}{d \ln V})$ , is the softening effect due to the  $s$ -to- $d$  electronic transition. The term  $\frac{\delta \varepsilon}{\delta \ln S}$  describes the average change in one-electron energy per electron and exhibits a smooth change in volume [12]. The term  $n_s$  depends on the finer details of the band structure. When the term  $dn_s$  in Mo experiences an anomaly around 50 GPa, the bulk modulus ( $B$ ) displays an anomaly at the same pressure [12]. The bulk modulus ( $B$ ), longitudinal sound velocity ( $C_L$ ), and shear modulus ( $G$ ) are then related by the following equation [28]:

$$B = \rho C_L^2 - \frac{4}{3}G, \quad (7)$$

where  $\rho$  is the material density. The  $s$ -to- $d$  transition rate in the primary stage is high, but it diminishes gradually when the pressure is higher than 50 GPa [Figs. 5(a) and 5(b)]. Thus, the shear modulus and the longitudinal sound velocity both show an anomaly at  $\sim 50$  GPa [27,32,64]. Therefore, the

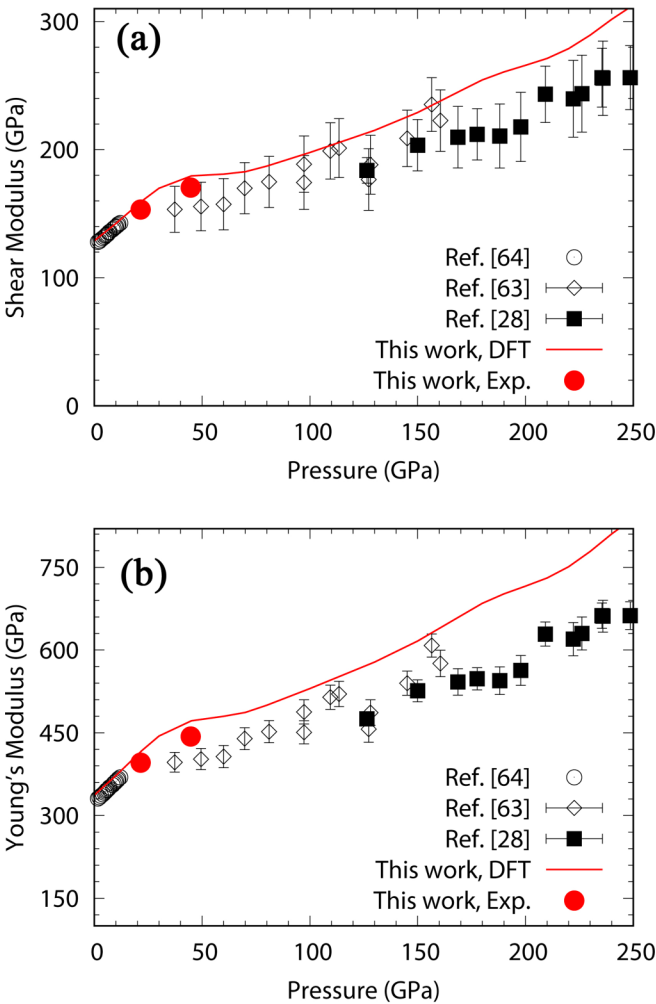


FIG. 4. Elastic moduli of solid Mo at high pressures. Shear modulus (a) and Young's modulus (b) of Mo when under high pressure. Solid red circles represent our experimental results, and the solid red line is for our DFT calculations. The hollow circles represent the results reported from Ref. [64] at high pressures and room temperatures. Diamonds (Ref. [63]) and squares (Ref. [28]) represent results from shock-wave experiments.

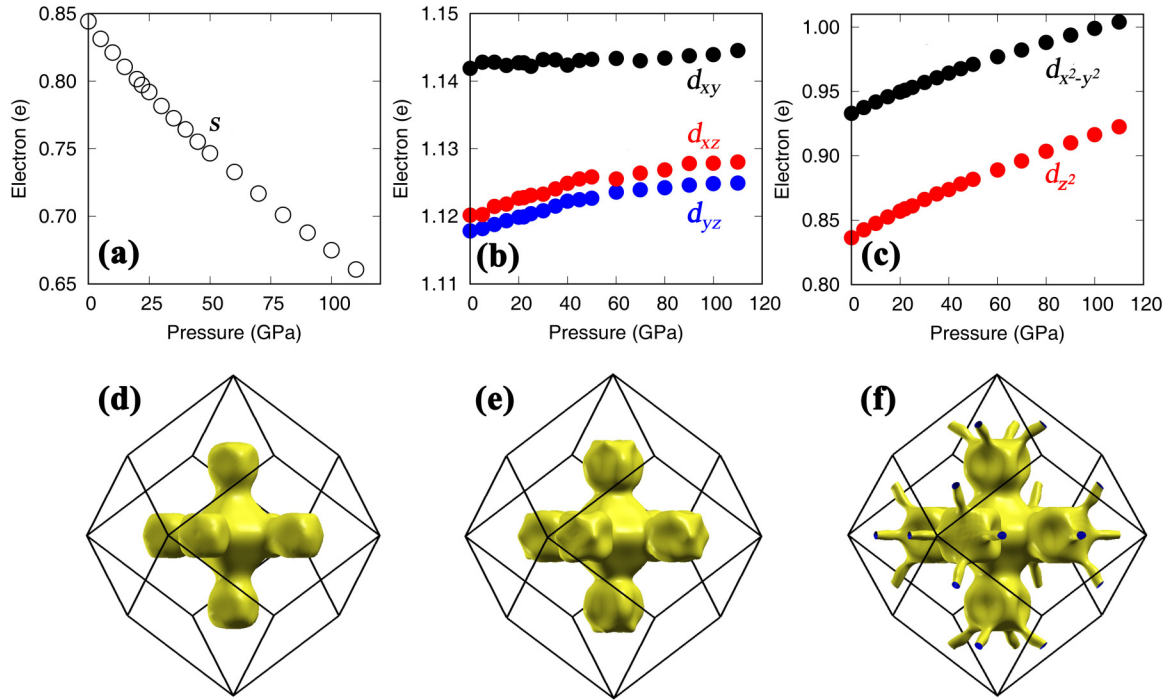


FIG. 5. Number of electrons and 3D Fermi surfaces of Mo calculated using VASP at high pressure. Number of electrons of  $s$  orbital (a) and  $d$  orbital (b), (c) as a function of pressure. Three-dimensional Fermi surface of Mo at 0 (d), 110 (e), and 210 (f) GPa. Fermi surfaces in panel (f) show an occurrence of an electronic topological transition at  $\sim 210$  GPa (blue areas). Three-dimensional Fermi surfaces were visualized using the XCRYSDEN package [50].

elastic moduli anomaly of bcc-Mo, which is around 50 GPa, originates from the  $s$ -to- $d$  electronic transition.

We further calculated the 3D Fermi surface structure of Mo up to 210 GPa (another band that crosses into the Fermi level), which has a six-sided cubiclelike structure elongated along the  $\Gamma$ - $H$  direction [Figs. 5(d)–5(f)], to better understand the mechanism of the elastic anomaly at around 210 GPa indicated by the previous shock experiments as well as our DFT calculations (Fig. 4). The topology of the Fermi surfaces exhibits no change up to 110 GPa. However, the corners of the cubiclelike structures become sharper and extrude out gradually with a further increase in pressure. About 210 GPa, these features become small cylindrical channels that bridge the 3D Fermi-surface structures in different Brillouin zones, and this eventually leads to a Lifshitz-type electronic topological transition.

The ETT-induced elastic anomalies can be described by a previously reported model (Ref. [26]). For a critical energy  $E_c$  where the Fermi surface undergoes an ETT, the ETT contribution to the elastic constants ( $C_{ij}$ ) can be approximately described by the following equation [26]:

$$C_{ij} = \frac{1}{V} \frac{\partial^2 E_{\text{band}}}{\partial \varepsilon_i \partial \varepsilon_j} \approx \frac{1}{4\pi^2 V |E^*|^{3/2}} \left[ -\frac{E_F}{2} \Delta E^{-(1/2)} \right] \frac{\partial^2 \Delta E}{\partial \varepsilon_i \partial \varepsilon_j}, \quad (8)$$

where  $E_{\text{band}}$  is the band contribution from ETT to the total energy, and  $V$  is the volume.  $E_F$  is the energy of the Fermi level;  $\varepsilon_i$  and  $\varepsilon_j$  are the strain components;  $E^*$  is a constant parameter;  $\Delta E = E_F - E_c$ . When ETT occurs, the difference between  $E_F$  and  $E_c$  reaches a minimum, and thus,  $C_{ij}$  can decrease suddenly. Upon increasing the pressure beyond ETT,

$E_F$  moves away from  $E_c$ ; thus, the contribution grows weaker, and  $C_{ij}$  returns to normal behavior [26,70]. This phenomenon is similar to other observations in bcc-Ta at  $\sim 100$  GPa or bcc-Nb at  $\sim 350$  GPa [17,18,71]. Therefore, the elastic modulus anomaly in Mo at  $\sim 210$  GPa can be associated with the occurrence of the ETT [28,72–74]. We note that there exist some controversies in the interpretations of the high  $P$ - $T$  phase diagram and physical properties of Mo in both experimental and computational results [25,27,32,72,75,76]. Based on our calculations, the ETT occurs at 210 GPa and 0 K [28–30,32,55]. However, since the elastic anomaly located around 210 GPa in DFT calculations may not occur at high pressure-temperature [55,65], future theoretical and experimental studies are needed to help decipher the correlation between the elastic softening, electron-phonon coupling anomalies, and phase diagram of Mo at high  $P$ - $T$ . ETT mostly correlates to the electronic structures around the Fermi level. Therefore, we calculated the  $d$ -orbital projected 3D Fermi surfaces, and the results are shown in Figs. 6(a)–6(e). It is clear that ETT at high pressures are mostly due to the  $d_{yz}$  orbital. Additionally, the calculated  $d$ -orbital projected 3D Fermi-surface structures of eighth band [Figs. 6(f)–6(j)] indicates that the Fermi-surface nesting effects under high pressures are mostly related to the  $d_{x^2-y^2}$  orbital.

Early in 1959, Kohn first discovered the Kohn anomaly in metallic systems that is related to the existence of a sharp Fermi surface [77]. Later, Peierls proved that the lattice structure of a one-dimensional system with a partially filled band becomes unstable as a result of a Kohn anomaly that is caused by a charge-density wave [78]. In 3D metallic systems, Kohn anomalies are weak and do not always cause any lattice

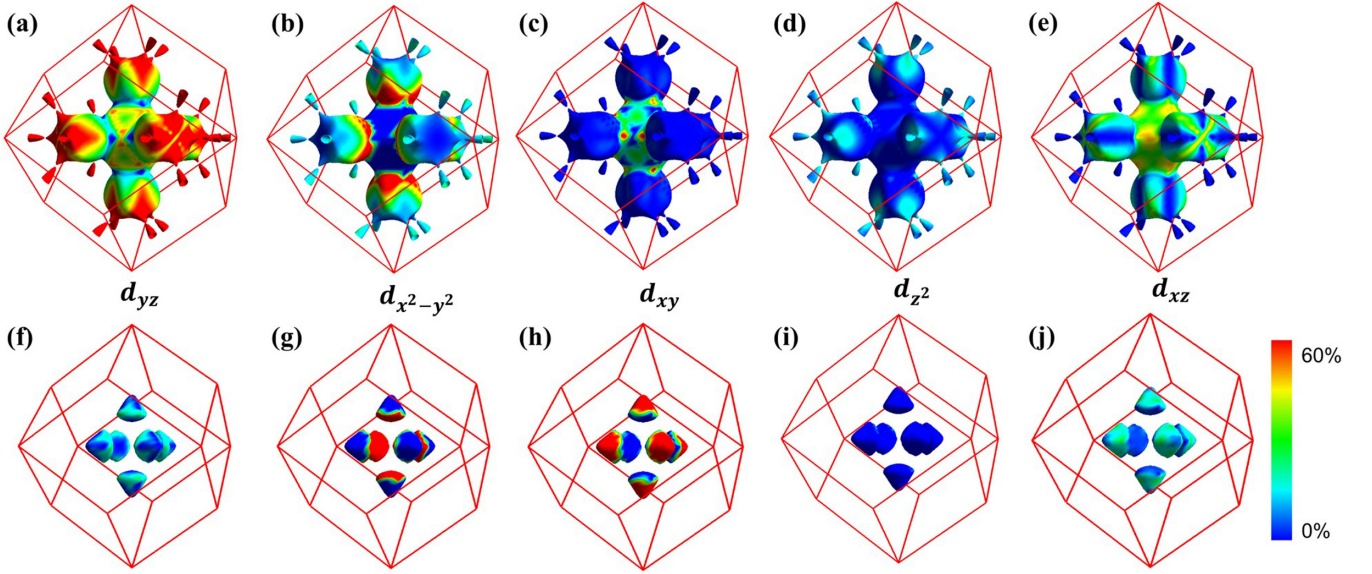


FIG. 6.  $d$ -Orbital projected 3D Fermi surfaces of bcc Mo at 210 GPa calculated using QUANTUM ESPRESSO. Corresponding  $d$ -orbital projected 3D Fermi surfaces of seventh band (a)–(e) and eighth band (f)–(j). The  $s$ - and  $p$  orbitals are ignored because they have small contributions near the Fermi level.  $d$ -Orbital projected 3D Fermi surfaces were displayed using FERMISURFER [54].

instabilities [79]. However, because a Kohn anomaly is closely related to the Fermi-surface nesting and electron-phonon coupling, it is usually described as a superconductivity signal [80]. As described earlier, a few  $d$ -block transition metals exhibit phonon Kohn anomalies at ambient or under high pressure [81]. In this study, we found a phonon anomaly beyond the  $H$  point along the  $\Gamma$ - $H$  direction in bcc-Mo. This finding is similar to that in other typical bcc crystal structures, such as V, Ta, and Nb which are adjacent to Mo on the periodic table [81]; however, their phonons at the  $H$  point do not show any anomalies under ambient or high-pressure conditions [19]. Our results here may help advance the understanding of previous observations that V, Ta, and Nb all have a nonmonotonic pressure dependence on superconducting transition temperature, whereas the superconducting transition temperature of Mo seems to decrease with an increase in pressure [6].

The crystal structures of elemental metals tend to occur in certain sequences when they are viewed as a function of atomic number or hydrostatic pressure, and this can be understood in terms of changes in  $d$ -band occupations [10]. However, in 2007, the structural phase transition of V was observed at 69 GPa; it was proposed that this was driven by the softening of the  $C_{44}$  trigonal elasticity tensor, which originates from the combination of Fermi-surface nesting, band Jahn-Teller distortion, and ETT. This mechanism is contrary to the  $s$ -to- $d$  electronic transition mechanism [15]. Since that study, many studies have shown that the elastic modulus anomalies of Nb and Ta at high pressures also have a similar mechanism that is driven like that of V [16,18,81].

In summary, the phonon Kohn anomaly, band Jahn-Teller distortions, and ETT are mostly related to the modifications and interactions of  $d$  orbitals in  $d$ -block transition metals under compression. ETT and elastic modulus anomalies are correlated through  $d_{yz}$  orbitals, and the Kohn anomalies at  $q \sim 0.5$  mostly correspond to the  $d_{x^2-y^2}$  orbital. Therefore, applying pressure as well as chemical and electron doping can

be used to modulate  $d$  orbitals, leading to the Kohn anomaly, ETT, and the elastic moduli anomaly. Our studies are useful for advancing the understanding of complex properties of typical bcc transition metals, such as Nb, Cr, and Fe [81,82].

#### IV. CONCLUSIONS

In conclusion, we used inelastic x-ray scattering experiments and density-functional theory calculations to determine the lattice vibrations and mechanical properties of bcc Mo at high pressures. Phonon dispersions along the high-symmetric directions were measured up to  $\sim 45$  GPa at quasi-hydrostatic compression and calculated up to 210 GPa using DFT. Kohn anomalies were observed in acoustic LA mode along the  $\Gamma$ - $H$  direction when under high pressure, and these change with an increase in pressure. The Kohn anomaly near the  $H$  point decreased with an increase in pressure, and this is due to the pressure-decreased magnitude of the electron-phonon coupling coefficient. Our calculations indicate that at high pressures, the Kohn anomaly at  $q \sim 0.5$  along the longitudinal acoustic phonon branch is induced by the enhanced Fermi-surface nesting effect. Further calculated projected 3D Fermi surfaces indicate that the topological structure of the  $d_{x^2-y^2}$  orbital contributes to the Kohn anomalies. Elastic modulus anomalies in Mo were observed in both experiments and calculations at pressures of  $\sim 50$  and 210 GPa. Our first-principles calculations show that the elastic anomaly at  $\sim 50$  GPa is caused by the abrupt change of the transition rate of  $s$ -to- $d_{xz}/d_{yz}$  electronic transition on compression; in contrast, the elastic anomaly at  $\sim 210$  GPa results from the electronic topological transition and is mostly due to the  $d_{yz}$  orbital. Our study helps to advance the understanding of lattice dynamic properties of Mo and may shed light on unusual elasticity in other bcc transition metals under extreme conditions.

## ACKNOWLEDGMENTS

We acknowledge support from the National Natural Science Foundation of China (NSFC) (Grants No. 11872077 and No. U1930401). C.Y. acknowledges support from the Natural Science Fund Project of Hunan Province, China (Grant No. 2020JJ5453) and the Scientific Research Fund of Hunan Provincial Education Department, China (Grant No. 20B487). Y.Z. acknowledges support from the National Key R&D Program of China (Grant No. 2017YFA0303600). The authors are grateful to Y. P. Yang and Z. L. Fan for generous supports on the FIB cutting at HPSTAR. Theoretical calculations were

performed using resources of the Texas Advanced Computing Center (TACC) at The University of Texas at Austin and the National Supercomputer Centre in Guangzhou. N.P.S. acknowledges support by the DOE-NNSA under Grant No. DE-NA0003975 (Chicago/DOE Alliance Center). This research used resources of the Advanced Photon Source, a U.S. Department of Energy (DOE) Office of Science User Facility operated for the DOE Office of Science by Argonne National Laboratory under Contract No. DEAC02-06CH11357. We thank GSECARS, APS for providing XRD and HPCAT, APS for their optical ruby system facilities in this study.

- [1] F. Poitrasson, A. N. Halliday, D. Lee, S. Levasseur, and N. Teutsch, *Earth Planet. Sci. Lett.* **223**, 253 (2004).
- [2] J. Lin, D. L. Heinz, A. J. Campbell, J. M. Devine, and G. Shen, *Science* **295**, 313 (2002).
- [3] D. Alfe, *Phys. Rev. B* **79**, 060101(R) (2009).
- [4] Y. Zhang, Y. Tan, H. Y. Geng, N. P. Salke, Z. Gao, J. Li, T. Sekine, Q. Wang, E. Greenberg, V. B. Prakapenka, and J.-F. Lin, *Phys. Rev. B* **102**, 214104 (2020).
- [5] S. Tateno, K. Hirose, Y. Ohishi, and Y. Tatsumi, *Science* **330**, 359 (2010).
- [6] J. Hamlin, *Physica C (Amsterdam, Neth.)* **514**, 59 (2015).
- [7] P. Parisiades, *Crystals* **11**, 416 (2021).
- [8] H. Xia, S. J. Duclos, A. L. Ruoff, and Y. K. Vohra, *Phys. Rev. Lett.* **64**, 204 (1990).
- [9] P. F. McMillan, *Nat. Mater.* **1**, 19 (2002).
- [10] H. L. Skriver, *Phys. Rev. B* **31**, 1909 (1985).
- [11] J. M. Wills, O. Eriksson, P. Soderlind, and A. M. Boring, *Phys. Rev. Lett.* **68**, 2802 (1992).
- [12] A. K. McMahan, H. L. Skriver, and B. Johansson, *Phys. Rev. B* **23**, 5016 (1981).
- [13] Y. Vohra, S. Sikka, and W. Holzapfel, *J. Phys. F: Met. Phys.* **13**, L107 (1983).
- [14] W. Luo, R. Ahuja, Y. Ding, and H. K. Mao, *Proc. Natl. Acad. Sci. USA* **104**, 16428 (2007).
- [15] Y. Ding, R. Ahuja, J. Shu, P. Chow, W. Luo, and H.-k. Mao, *Phys. Rev. Lett.* **98**, 085502 (2007).
- [16] D. Antonangeli, D. L. Farber, A. H. Said, L. R. Benedetti, C. M. Aracne, A. Landa, P. Söderlind, and J. E. Klepeis, *Phys. Rev. B* **82**, 132101 (2010).
- [17] Y. X. Wang, H. Y. Geng, Q. Wu, X. R. Chen, and Y. Sun, *J. Appl. Phys.* **122**, 235903 (2017).
- [18] Y. Zhang, C. Yang, A. Alatas, A. H. Said, N. P. Salke, J. Hong, and J.-F. Lin, *Phys. Rev. B* **100**, 075145 (2019).
- [19] D. L. Farber, M. Krisch, D. Antonangeli, A. Beraud, J. Badro, F. Occelli, and D. Orlikowski, *Phys. Rev. Lett.* **96**, 115502 (2006).
- [20] A. D. B. Woods and S. H. Chen, *Solid State Commun.* **2**, 233 (1964).
- [21] A. D. B. Woods and B. M. Powell, *Phys. Rev. Lett.* **15**, 778 (1965).
- [22] J. Zarestky, C. Stassis, B. N. Harmon, K. M. Ho, and C. L. Fu, *Phys. Rev. B* **28**, 697 (1983).
- [23] R. Bauer, A. Schmid, P. Pavone, and D. Strauch, *Phys. Rev. B* **57**, 11276 (1998).
- [24] A. B. Belonoshko, S. I. Simak, A. E. Kochetov, B. Johansson, L. Burakovsky, and D. L. Preston, *Phys. Rev. Lett.* **92**, 195701 (2004).
- [25] A. B. Belonoshko, L. Burakovsky, S. P. Chen, B. Johansson, A. S. Mikhaylushkin, D. L. Preston, S. I. Simak, and D. C. Swift, *Phys. Rev. Lett.* **100**, 135701 (2008).
- [26] L. Koči, Y. Ma, A. Oganov, P. Souvatzis, and R. Ahuja, *Phys. Rev. B* **77**, 214101 (2008).
- [27] R. S. Hixson, D. A. Boness, J. W. Shaner, and J. A. Moriarty, *Phys. Rev. Lett.* **62**, 637 (1989).
- [28] J. H. Nguyen, M. C. Akin, R. Chau, D. E. Fratanduono, W. P. Ambrose, O. V. Fat'yanov, P. D. Asimow, and N. C. Holmes, *Phys. Rev. B* **89**, 174109 (2014).
- [29] J. H. Nguyen, M. C. Akin, R. Chau, D. E. Fratanduono, W. P. Ambrose, O. V. Fat'yanov, P. D. Asimow, and N. C. Holmes, *Phys. Rev. B* **92**, 026102 (2015).
- [30] C. Cazorla, D. Alfè, and M. J. Gillan, *Phys. Rev. Lett.* **101**, 049601 (2008).
- [31] S. Taioli, C. Cazorla, M. J. Gillan, and D. Alfè, *Phys. Rev. B* **75**, 214103 (2007).
- [32] D. Errandonea, R. Boehler, and M. Ross, *Phys. Rev. B* **92**, 026101 (2015).
- [33] J. Wang, F. Coppari, R. F. Smith, J. H. Eggert, A. E. Lazicki, D. E. Fratanduono, J. R. Rygg, T. R. Boehly, G. W. Collins, and T. S. Duffy, *Phys. Rev. B* **92**, 174114 (2015).
- [34] L. Lei, B. Yan, and X. Ji-An, *Chin. Phys. B* **22**, 056201 (2013).
- [35] X. Huang, F. Li, Q. Zhou, Y. Meng, K. D. Litasov, X. Wang, B. Liu, and T. Cui, *Sci. Rep.* **6**, 19923 (2016).
- [36] A. H. Said, H. Sinn, T. S. Toellner, E. E. Alp, T. Gog, B. M. Leu, S. Bean, and A. Alatas, *J. Synchrotron Radiat.* **27**, 827 (2020).
- [37] T. Toellner, A. Alatas, and A. Said, *J. Synchrotron Radiat.* **18**, 605 (2011).
- [38] E. Burkel, *Rep. Prog. Phys.* **63**, 171 (2000).
- [39] H. Sinn, *J. Phys.: Condens. Matter* **13**, 7525 (2001).
- [40] A. H. Said, H. Sinn, and R. Divan, *J. Synchrotron Radiat.* **18**, 492 (2011).
- [41] R. T. Azuah, L. R. Kneller, Y. Qiu, P. L. Tregenna-Piggott, C. M. Brown, J. R. Copley, and R. M. Dimeo, *J. Res. Natl. Inst. Stand.* **114**, 341 (2009).
- [42] G. Kresse and J. Hafner, *Phys. Rev. B* **47**, 558 (1993).
- [43] G. Kresse, J. Furthmüller, and J. Hafner, *Europhys. Lett.* **32**, 729 (1995).
- [44] To ensure the accuracy of the interatomic forces, we used an energy convergence criterion of  $10^{-6}$  eV and a maximum Hellmann-Feynman force on each atom less than  $10^{-3}$  eV Å<sup>-1</sup>.
- [45] A. Togo, F. Oba, and I. Tanaka, *Phys. Rev. B* **78**, 134106 (2008).
- [46] G. Kresse and J. Furthmüller, *Comput. Mater. Sci.* **6**, 15 (1996).
- [47] G. Kresse and J. Furthmüller, *Phys. Rev. B* **54**, 11169 (1996).

- [48] S. Maintz, V. L. Deringer, and R. Dronskowski, *J. Comput. Chem.* **34**, 2557 (2013).
- [49] A. A. Mostofi, J. R. Yates, G. Pizzi, Y.-S. Lee, I. Souza, D. Vanderbilt, and N. Marzari, *Comput. Phys. Commun.* **185**, 2309 (2014).
- [50] A. Kokalj, *Comput. Mater. Sci.* **28**, 155 (2003).
- [51] K. F. Garrity, J. W. Bennett, K. M. Rabe, and D. Vanderbilt, *Comput. Mater. Sci.* **81**, 446 (2014).
- [52] X. Gonze, B. Amadon, P.-M. Anglade, J.-M. Beuken, F. Bottin, P. Boulanger, F. Bruneval, D. Caliste, R. Caracas, and M. Côté, *Comput. Phys. Commun.* **180**, 2582 (2009).
- [53] P. Giannozzi, S. Baroni, N. Bonini, M. Calandra, R. Car, C. Cavazzoni, D. Ceresoli, G. L. Chiarotti, M. Cococcioni, and I. Dabo, *J. Phys.: Condens. Matter* **21**, 395502 (2009).
- [54] M. Kawamura, *Comput. Phys. Commun.* **239**, 197 (2019).
- [55] See Supplemental Material at <http://link.aps.org/supplemental/10.1103/PhysRevB.105.094105> for the calculation details for Mo with different energy-cutoff and k-point meshes, and the Fermi surfaces of Mo at high P-T conditions.
- [56] B. Powell, P. Martel, and A. Woods, *Phys. Rev.* **171**, 727 (1968).
- [57] F. Giustino, *Rev. Mod. Phys.* **89**, 015003 (2017).
- [58] D. Lamago, M. Hoesch, M. Krisch, R. Heid, K. P. Bohnen, P. Boni, and D. Reznik, *Phys. Rev. B* **82**, 195121 (2010).
- [59] K. W. Böer and U. W. Pohl, *Semiconductor Physics* (Springer, Berlin, Heidelberg, 2018).
- [60] L. Louail, D. Maouche, A. Roumili, and F. A. Sahraoui, *Mater. Lett.* **58**, 2975 (2004).
- [61] O. Krasilnikov, M. Belov, A. Lugovskoy, I. Y. Mosyagin, and Y. K. Vekilov, *Comput. Mater. Sci.* **81**, 313 (2014).
- [62] M. Ganchenkova and R. M. Nieminen, in *Handbook of Silicon Based MEMS Materials and Technologies*, 2nd ed. (Elsevier Inc., 2015), p. 253.
- [63] X. Zhang, Z. Liu, K. Jin, F. Xi, Y. Yu, Y. Tan, C. Dai, and L. Cai, *J. Appl. Phys.* **117**, 054302 (2015).
- [64] W. Liu, Q. Liu, M. L. Whitaker, Y. Zhao, and B. Li, *J. Appl. Phys.* **106**, 043506 (2009).
- [65] T. Lukinov, S. I. Simak, and A. B. Belonoshko, *Phys. Rev. B* **92**, 060101(R) (2015).
- [66] J. A. Moriarty, *Phys. Rev. B* **45**, 2004 (1992).
- [67] B. K. Godwal and R. Jeanloz, *Phys. Rev. B* **41**, 7440 (1990).
- [68] O. Andersen, J. Madsen, U. Poulsen, O. Jepsen, and J. Kollar, *Physica B+C* **86**, 249 (1977).
- [69] A. Mackintosh and O. Andersen, in *Electrons at the Fermi Surface*, edited by M. Springford (Cambridge University Press, London and New York, 1980), p. 149.
- [70] I. M. Lifshitz, *Sov. Phys. JETP* **11**, 1130 (1960).
- [71] Y. M. Blanter, M. Kaganov, A. Pantsulaya, and A. Varlamov, *Phys. Rep.* **245**, 159 (1994).
- [72] M. Ross, D. Errandonea, and R. Boehler, *Phys. Rev. B* **76**, 184118 (2007).
- [73] A. Salamat, R. Briggs, P. Bouvier, S. Petitgirard, A. Dewaele, M. E. Cutler, F. Cora, D. Daisenberger, G. Garbarino, and P. F. McMillan, *Phys. Rev. B* **88**, 104104 (2013).
- [74] R. Briggs, D. Daisenberger, O. T. Lord, A. Salamat, E. Bailey, M. J. Walter, and P. F. McMillan, *Phys. Rev. B* **95**, 054102 (2017).
- [75] D. Santamaría-Pérez, M. Ross, D. Errandonea, G. Mukherjee, M. Mezouar, and R. Boehler, *J. Chem. Phys.* **130**, 124509 (2009).
- [76] D. Errandonea, B. Schwager, R. Ditz, C. Gessmann, R. Boehler, and M. Ross, *Phys. Rev. B* **63**, 132104 (2001).
- [77] W. Kohn, *Phys. Rev. Lett.* **2**, 393 (1959).
- [78] R. E. Peierls, *Quantum Theory of Solids* (Oxford University Press, Oxford, 1955).
- [79] E. Woll Jr and W. Kohn, *Phys. Rev.* **126**, 1693 (1962).
- [80] P. Aynajian, T. Keller, L. Boeri, S. Shapiro, K. Habicht, and B. Keimer, *Science* **319**, 1509 (2008).
- [81] A. Landa, P. Söderlind, I. I. Naumov, J. E. Klepeis, and L. Vitos, *Computation* **6**, 29 (2018).
- [82] T. M. Rice and B. I. Halperin, *Phys. Rev. B* **1**, 509 (1970).